


Ferroelectric higher-order topological insulator in two dimensions

Ning Mao, Runhan Li, Xiaorong Zou, Ying Dai,^{*} Baibiao Huang, and Chengwang Niu[†]
School of Physics, State Key Laboratory of Crystal Materials, Shandong University, Jinan 250100, China

 (Received 1 August 2022; revised 11 December 2022; accepted 9 January 2023; published 18 January 2023)

The interplay between ferroelectricity and band topology can give rise to a wide range of both fundamental and applied research. Here, we map out the emergence of nontrivial corner states in two-dimensional ferroelectrics and, remarkably, demonstrate that ferroelectricity and corner states are coupled together by crystallographic symmetry to realize the electric control of higher-order topology. Implementing density functional theory, we identify a series of experimentally synthesized two-dimensional ferroelectrics, such as In_2Se_3 , BN, and SnS, as realistic material candidates for the proposed ferroelectric higher-order topological insulators. Our work not only sheds light on traditional ferroelectric materials but also opens an avenue to bridge the higher-order topology and ferroelectricity that provides a nonvolatile handle to manipulate the topology in next-generation electronic devices.

DOI: [10.1103/PhysRevB.107.045125](https://doi.org/10.1103/PhysRevB.107.045125)

I. INTRODUCTION

Time-reversal polarization, defined as the differences between Wannier charge centers of Kramers pair, plays a pivotal role in the \mathbb{Z}_2 classification of electronic topological insulators (TIs) [1–3]. Armed with topologically protected metallic boundary (surface or edge) states, TIs ensure the dissipationless nature of spin transport with promising applications in spintronics [4–7]. The existence of boundary-localized mass domains, as generally accepted, will open up a boundary band gap, thereby trivializing the time-reversal polarization in TIs. Remarkably, recent investigations proposed that hinge or corner states may appear, resulting in the intriguing quantum phase called higher-order TIs (HOTIs) [8–12]. In particular, as the expectation value of the position operator of Wannier functions, the quantized polarization can be topological indices for C_n -symmetric HOTIs, which form into \mathbb{Z}_2 , $\mathbb{Z}_2 \times \mathbb{Z}_2$, or \mathbb{Z}_3 indexes [13–15]. As a novel extension of TIs, theoretical models and material candidates of HOTIs have been proposed in both two and three dimensions [16–24] and, remarkably, have been experimentally observed in three-dimensional Bi [25], WTe_2 [26], and Bi_4Br_4 [27]. However, for two-dimensional (2D) electronic materials, the experimental confirmation of HOTIs has been elusive so far.

On the other hand, polarization has received great attention in relation to ferroelectric materials [28–39]. One important characteristic of ferroelectric materials is the existence of two degenerate structures with opposite polarizations that could be switched by an external electric field [40]. In fact, switchable electric polarization, when coupled to other properties such as ferromagnetism, ferroelasticity, valleys, skyrmions, spin polarization, and/or nontrivial band topology, provides a nonvolatile control with the implementation of gate

voltages [41–46]. Moreover, the separation of the centers of positive and negative electric charges in ferroelectric systems currently serves as a hallmark of obstructed atomic limits (OALs) within the framework of topological quantum chemistry theory [47,48]. OALs have recently attracted significant interest since they can manifest at the boundary in terms of metallic surface/edge states, regardless of spin-orbit coupling (SOC) or bulk band inversion [49–54]. Moreover, some of them could host hinge/corner states as a result of the filling anomaly, which leads to the higher-order topology. Therefore, a natural question arises as to whether ferroelectric polarization can result in the emergence of HOTIs, especially in two dimensions.

In the present work, we demonstrate the emergence of higher-order topological phases in 2D ferroelectrics, including both the in-plane and out-of-plane ferroelectricity. Moreover, we reveal that the in-plane polarizations, which can enforce the nonquantized ones and the quantized ones, enable the emergence of the corner states and may even serve as topological invariants. Effective models for both the quantized and nonquantized in-plane polarizations are constructed to demonstrate the feasibility of attaining the proposed 2D ferroelectric HOTIs. Remarkably, based on the first-principles calculations, a wide range of 2D ferroelectrics are found to possess fractional corner charges, resulting in higher-order topological phases, for which implementing an external electric field could switch the directions of ferroelectric polarization and in turn change the position of corner states and/or mediate the topological phase transitions. Our results indicate that 2D ferroelectric materials provide an up-and-coming platform to achieve and control higher-order corner states with experimentally feasible examples.

II. METHOD

First-principles calculations are carried out in the framework of the generalized gradient approximation with the

^{*}daiy60@sdu.edu.cn

[†]c.niu@sdu.edu.cn

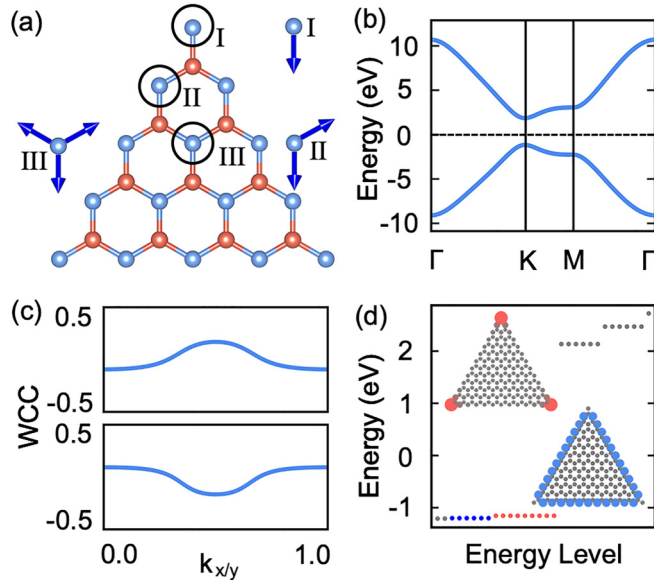


FIG. 1. (a) Sketch of the finite triangular lattice with C_3 symmetry. The quantized polarization in the bulk (III) can always be annihilated, whereas the edge (II) and corner (I) may possess uncompensated polarization. (b) Band structures of the two-band Hamiltonian. (c) The Wilson bands of the occupied band along the k_x (up) and k_y (down) directions. (d) Energy spectrum of the finite nanoflake. The red dots near the Fermi level represent the in-gap corner states, and the blue ones denote the edge states.

Perdew-Burke-Ernzerhof [55] functional using the Vienna Ab initio Simulation Package (VASP) [56] and the full-potential linearized augmented plane-wave method using the FLEUR code [57]. The self-consistent total energy was evaluated with a $12 \times 12 \times 1$ k -point mesh, and the cutoff energy for the plane-wave basis set was 500 eV. Maximally localized

Wannier functions are constructed using the WANNI90 code in conjunction with the FLEUR package [58–60], and van der Waals corrections as parameterized in the semiempirical density functional theory (DFT-D2) method are included. The Wilson loop calculations were done using WANNIERTOOLS [61], and the irreducible representations were done using IRVSP [62]. Moreover, the climbing image nudged elastic band method was used to determine the energy barriers of the phase transition.

III. MODEL RESULTS

A. First model Hamiltonian for quantized polarization

It has long been known that polarization is closely related to the position of the Wannier function, which can be transformed into the Berry phase of the occupied bands as

$$\mathbf{P} = -\frac{1}{2\pi} \int_k^{k+2\pi} \text{Tr}[\mathcal{A}_k] dk = -\frac{1}{2\pi} \phi. \quad (1)$$

Here, A_k is the gauge-dependent Berry connection in terms of $[\mathcal{A}_k]^{mn} = -i\langle u_k^m | \partial_k | u_k^n \rangle$, and its integral along a closed path is called the Berry phase ϕ . The direction of polarization is determined by the movement of the Wannier function, and the polarization can be quantized or nonquantized, limited by the crystal symmetry. Remarkably, as we demonstrate below, an in-plane polarization, whether it is quantized or nonquantized, will give rise to the two-dimensional higher-order corner states.

We consider first the quantized polarization in a two-band tight-binding model on a honeycomb lattice,

$$H = \sum_i \lambda_i c_i^\dagger c_i + t_1 \sum_{\langle ij \rangle} c_i^\dagger c_j + t_2 \sum_{\langle\langle ij \rangle\rangle} c_i^\dagger c_j. \quad (2)$$

The first term is the sublattice potential, which is needed to break inversion symmetry \mathcal{I} . The second and third terms represent the nearest- and next-nearest-neighbor hoppings, as

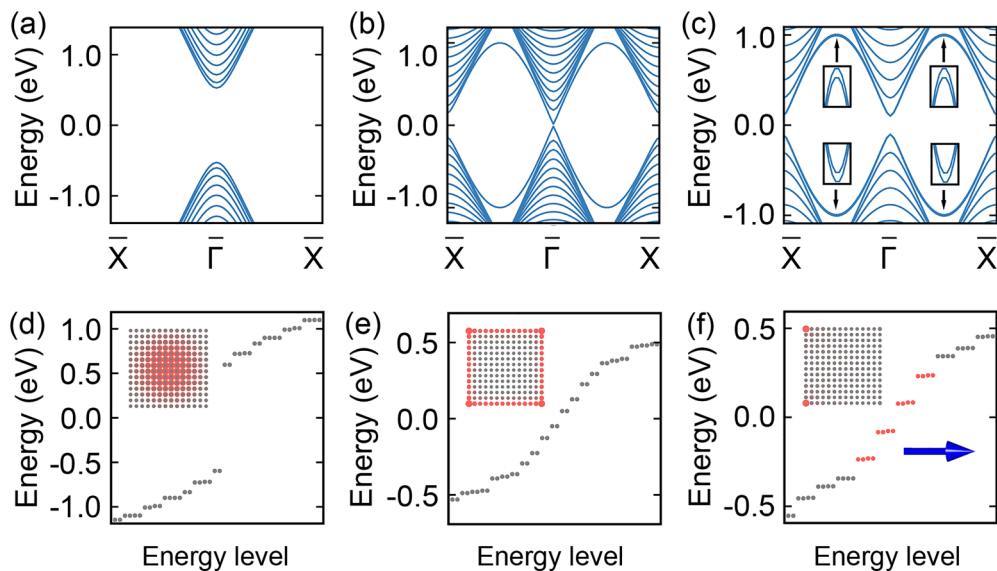


FIG. 2. Edge spectra of the tight-binding model under (a) trivial ($m = 2.5t$, $F = 0$), (b) nontrivial ($m = 0.2t$, $F = 0$), and (c) higher-order phases ($m = 0.2t$, $F = 0.001t$); parameters t and λ are set to 1. Energy spectrum of finite nanoflakes for (d) trivial, (e) nontrivial, and (f) higher-order phases. The red dots near the Fermi level represent the in-gap corner states, the blue arrow denotes the direction of the electric potential, and the distributions of corner, edge, and bulk states are plotted in the inset.

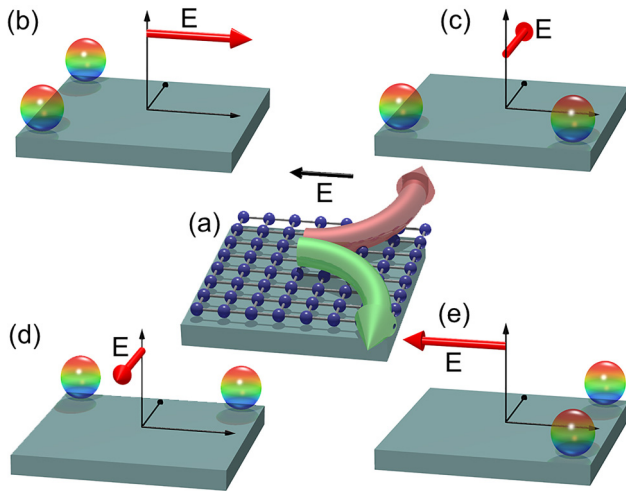


FIG. 3. (a) In-plane polarization and (b)–(e) corner states under the in-plane electric field. A transverse current is generated under in-plane electric field, which leads to the in-plane polarization and then the birth of corner states in symmetric corners. Corner states are indicated with rainbow balls, and arrows denote the directions of the in-plane electric field.

depicted in Fig. 1(a). In Fig. 1(b), we show the band structures of the Hamiltonian in the OAL phase. Indeed, the moving of Wannier charge centers leads to a quantized polarization, as shown by Fig. 1(c). However, the sum of the polarization, bounded by C_3 symmetry, can necessarily be zero in the bulk because $\mathbf{P}_{\text{bulk}} = \sum_i (\mathbf{P}_i + C_3 \mathbf{P}_i + C_3^{-1} \mathbf{P}_i) = 0$, while ones at the edges and corners cannot be offset as displayed in Fig. 1(a), leading to the nonvanishing polarization as $\mathbf{P}_{\text{edge}} = \sum_i (\mathbf{P}_i + C_3 \mathbf{P}_i)$ and $\mathbf{P}_{\text{corner}} = \sum_i \mathbf{P}_i$. Hence, electrons from the bulk will be driven to the edges and corners, forming the edge and corner states. Figure 1(d) presents the energy level of a finite triangular flake. Clearly, the edge and corner states emerge near the Fermi level. Moreover, corner states originating from the valence and conduction bands are degenerated in energy, giving rise to the phenomenon of the filling anomaly. In that sense, the corner states can be pushed into the conduction or valence bands as a whole, and the positive or negative charge will be generated to affect the charge neutrality.

B. Second model Hamiltonian for nonquantized polarization

For better control of the corner states, the nonquantized polarization has to be introduced by breaking the C_6 , C_4 , and C_3 symmetries. To study systematically the switchable corner

states, we then focus on a simple model of one atom located at the center of a 2D square lattice [16], and the Hamiltonian can be expressed as

$$H_0 = [m - t(\cos k_x + \cos k_y)]\tau_z - \lambda(\sin k_x \sigma_x + \sin k_y \sigma_y)\tau_x, \quad (3)$$

where m sets the energy offset between the s and p orbitals. SOC, denoted by λ , induces their hybridization, while the nearest-neighbor hopping t bridges the relations for s - s or p - p orbitals. The nonquantized polarization affects the electric potential of the system and causes a potential imbalance for the overall system. In this sense, we add an electric potential term to mimic the nonquantized polarization

$$H_E = \sum_i c_i^\dagger [eF(x \cos \theta + y \sin \theta)]c_i, \quad (4)$$

where $c_i^\dagger = (c_{i\uparrow}^\dagger, c_{i\downarrow}^\dagger)$ are electron creation operators at site i . Besides the elementary charge e , H_E is expressed with the amplitude given by F and orientation defined by θ . It is clear that, for an in-plane electric potential along the \hat{y} direction, the \mathcal{I} , C_6 , C_4 , C_3 , and C_{2x} (C_{2y}) symmetries are broken, and remarkably, as illustrated in Fig. 2, one can find that the corner states appear, serving as a direct signal of HOTIs.

However, the in-gap corner states appear only at specific corners, inspiring us to understand their physical origin. Since the in-plane electric fields induce the phase transition between the topological insulator and higher-order topological insulator, electrons from the bulk or edges will accumulate in the corners that would be accompanied by a transverse velocity, as schematically shown in Fig. 3(a). To map out the role of rotation symmetry and polarization, we choose four representatives with different in-plane orientations, where the rotation symmetries are highly sensitive to the orientations. In the absence of the electric potential, the considered square lattice has both $C_{2x} = -i\sigma_x$ and $C_{2y} = -i\sigma_y$, but no polarization and thus no corner states (see Fig. 2). If an electric potential is perpendicular to the \hat{x} (\hat{y}) direction, C_{2y} (C_{2x}) will be broken, and otherwise, it will be conserved. For example, in Fig. 3(b), C_{2y} is broken, while C_{2x} survives and ensures the existence of corner states. Interestingly, the in-gap corner states can be turned into opposite corners when the in-plane electric field and the polarization are reversed, as shown in Fig. 3(e). Similar results with corner states localized on C_{2y} -symmetric positions are shown in Figs. 3(c) and 3(d). Therefore, one can realize nonvolatile control of the corner states.

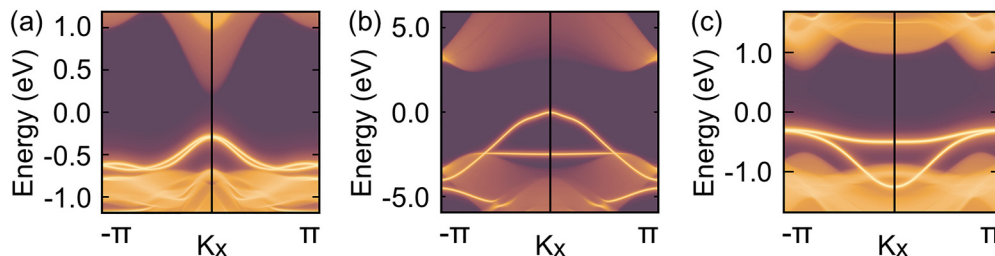


FIG. 4. Energy bands of the semi-infinite nanoribbon for (a) In_2Se_3 , (b) BN , and (c) SnS , revealing characteristic edge states for the higher-order topological phases.

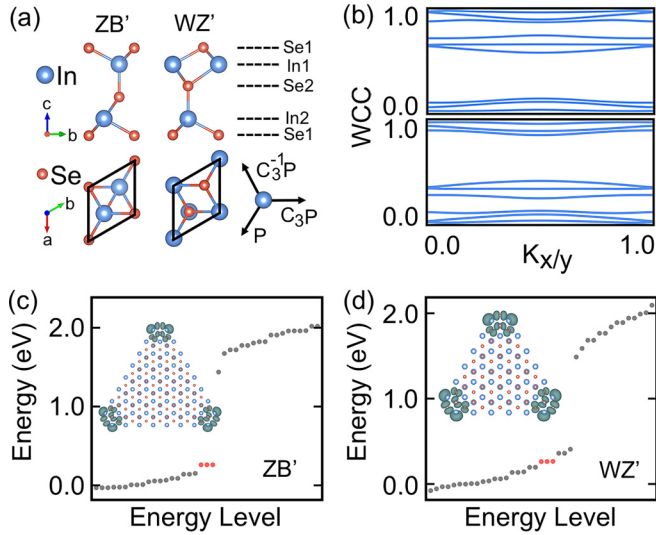


FIG. 5. (a) Top and side views of In_2Se_3 in the ZB' and WZ' phases. (b) Wilson bands of the occupied bands along the k_x (up) and k_y (down) directions. Energy spectra of In_2Se_3 in the (c) ZB' and (d) WZ' phases. The red dots near the Fermi level represent the in-gap corner states. Distributions of corner states are displayed in the insets.

IV. MATERIAL CANDIDATES

A. Traditional ferroelectrics

Having demonstrated the interplay of HOTIs and polarization, we aim now at its realization in electronic materials, where the in-plane polarization \mathbf{P} can be defined by

$$\mathbf{P} = p_1 \mathbf{a}_1 + p_2 \mathbf{a}_2. \quad (5)$$

Here, \mathbf{a}_1 and \mathbf{a}_2 are primitive lattice vectors, and the components p_1 and p_2 can serve as topological indices that

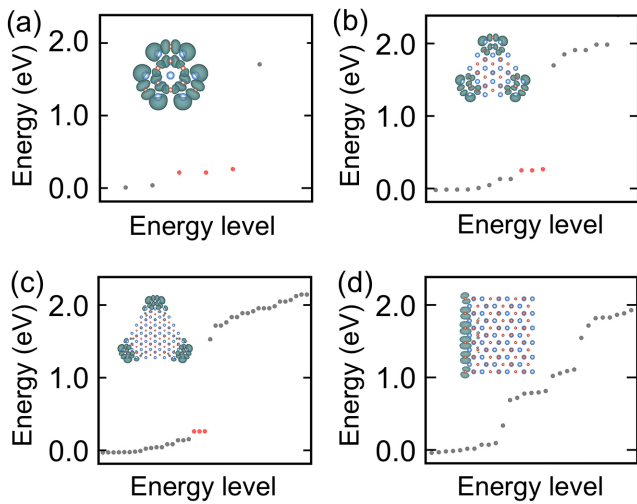


FIG. 6. Energy spectrum of the finite nanoflake for In_2Se_3 for sizes of (a) $4A$, (b) $6A$, and (c) $8A$, where A denotes the lattice constant. (d) Energy spectrum of the finite nanoflake in a rectangular shape for In_2Se_3 . The red dots near the Fermi level represent the in-gap corner states, and the distributions of edge and corner states are plotted in the inset.

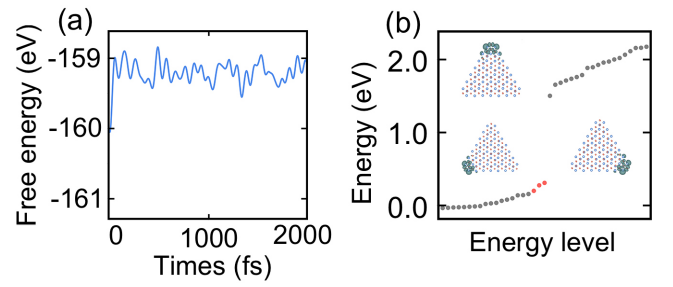


FIG. 7. (a) Variation of the free energy with 0–2000 fs for In_2Se_3 . The *ab Initio* molecular dynamics simulation is carried out with a $6 \times 6 \times 1$ supercell at 300 K. (b) Energy spectrum of the finite nanoflake for In_2Se_3 for the distorted structure. The red dots near the Fermi level represent the in-gap corner states, and the distributions of edge and corner states are plotted in the insets.

are equivalent to the quantized Berry phase [63]. Two-dimensional ferroelectric materials lack \mathcal{I} intrinsically and hence usually possess the electric polarization, which usually gives rise to gapped edge states (see Fig. 4), therefore revealing great opportunities for HOTIs in 2D ferroelectric materials. In addition, the ferroelectric nature has been demonstrated experimentally in abundant 2D layered materials, and indeed, ferroelectric switching is currently maturing into a significant burgeoning research topic; therefore, making a bridge between HOTIs and 2D ferroelectricity has great significance.

In_2Se_3 is one of the most famous examples of 2D ferroelectric materials and has been widely explored, with promising applications in phase-change memory, thermoelectrics, photoelectrics, and catalysis [64–68]. The monolayer is stacking, with a sequence of Se1-In1-Se2-In2-Se1 that can be easily realized by physical exfoliation and/or chemical vapor deposition. The modified zincblende (ZB') and wurtzite (WZ') phase of In_2Se_3 , as shown in Fig. 5(a), are the degenerate ground states, which have already been synthesized [69–71].

According to topological quantum chemistry theory and Wilson loop calculations, as illustrated in Fig. 5(b) [47,48], the valence bands of In_2Se_3 can be decomposed into a linear combination of elementary band representations,

$$4A_1 @ a + 2A_1 @ c + 2E @ a + E @ c. \quad (6)$$

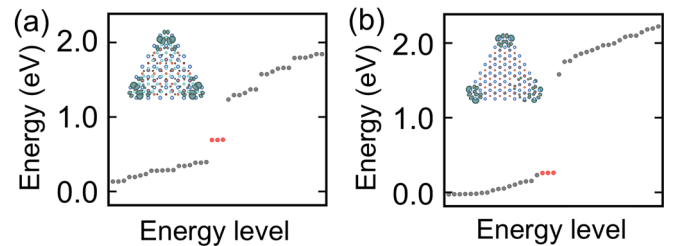


FIG. 8. Energy spectrum of the finite nanoflake for In_2Se_3 (a) for the SiC substrate and (b) with a deficiency of one In atom. The red dots near the Fermi level represent the in-gap corner states, and the distributions of corner states are plotted in the inset.

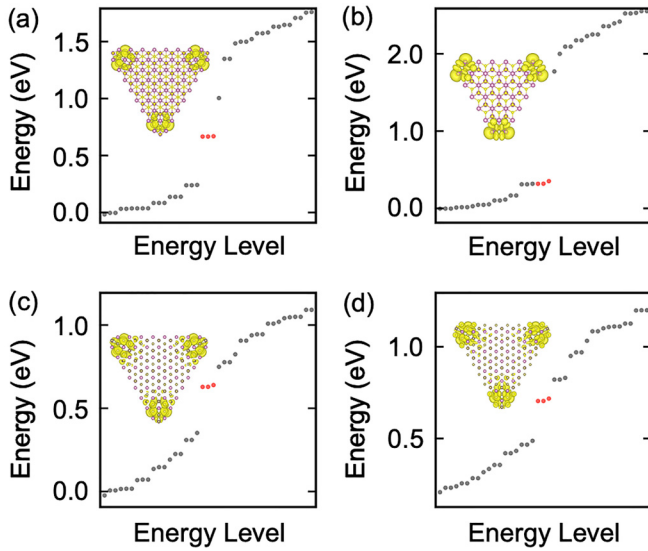


FIG. 9. Energy spectrum of finite nanoflakes for (a) and (b) In_2S_3 and (c) and (d) In_2Te_3 in the (a) and (c) ZB' and (b) and (d) WZ' phases. The red dots near the Fermi level represent the in-gap corner states, and the distributions of corner states are plotted in the inset.

Hence, the electron transfer occurs when atoms are brought together to form the crystal of In_2Se_3 , i.e., when the electrons of In move to Se, giving rise to the in-plane electric polarization. Limited by C_3 symmetry, the polarization induced by the electron distribution between In1/In2 and Se2 atoms can be quantized as

$$\mathbf{P} = (1/3, 1/3). \quad (7)$$

To further identify the nature of HOTIs, we construct a triangular nanoflake of In_2Se_3 which preserves the C_3 symmetry for both the bulk and edge. As plotted in Figs. 5(c) and 5(d), three degenerate in-gap states arise around the Fermi level, accumulating in three corners of Se2 atoms. The emergence

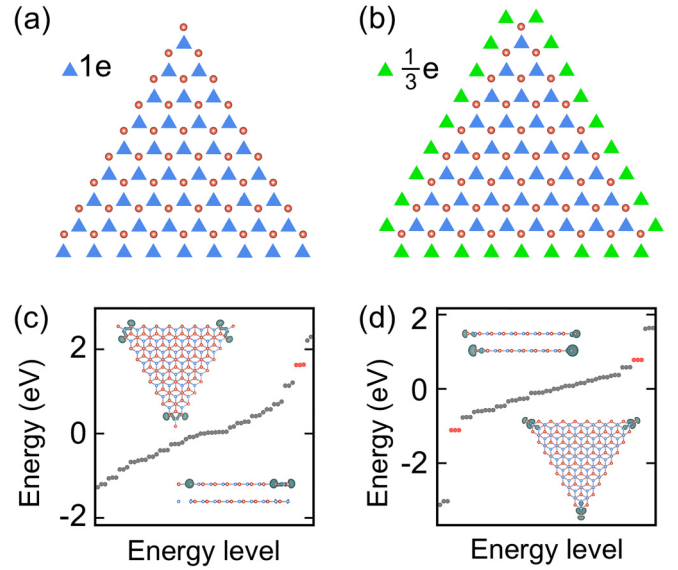


FIG. 11. (a) Nanoflake with atoms at the positions of the red circles, whose electrons are at the blue triangles. (b) Nanoflake formed by distributing the edge electrons averagely on three edges. Energy spectrums of the nanoflake for the BN bilayer in (c) AB stacking and (d) BA stacking. Red dots represent the in-gap corner states, and the distributions of corner states are plotted in the insets.

of corner states is robust against the perturbation of the size, temperature, substrate, and defects (see Figs. 6–8). In addition, such corner states also show up in the related systems of In_2S_3 and In_2Te_3 (see Fig. 9). However, the emergence of corner states between the ZB' and WZ' phases is nearly the same, making it difficult to control the corner states by an external electric field.

B. Sliding ferroelectrics

Aiming at revealing the nonvolatile control of corner states and the universality of pronounced ferroelectric HOTIs, we

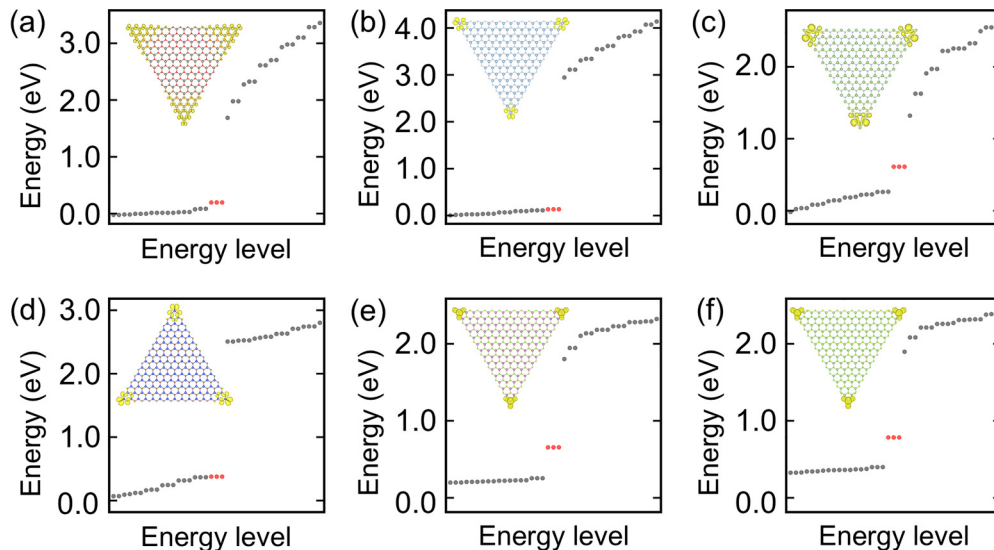


FIG. 10. Energy spectrum of finite nanoflakes for (a) ZnO, (b) AlN, (c) GaN, (d) SiC, (e) InSe, and (f) GaSe. The red dots near the Fermi level represent the in-gap corner states, and the distributions of corner states are plotted in the inset.

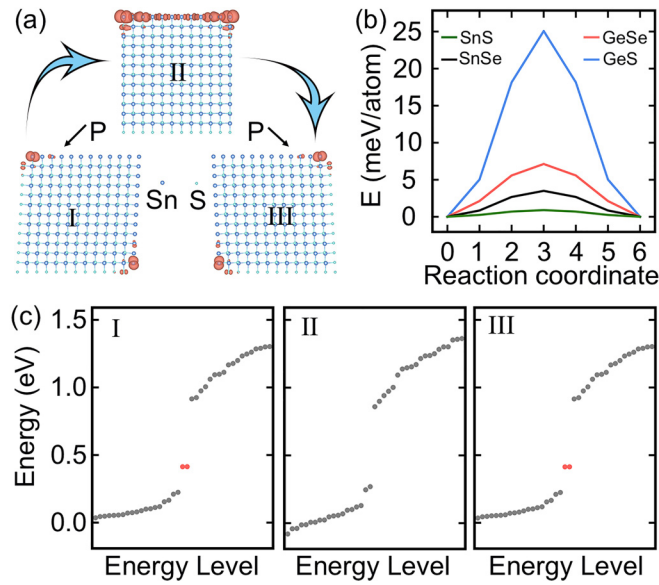


FIG. 12. (a) Distributions of corner states for ferroelastic states I and III and intermediate state II of SnS. (b) Energy profile of the kinetic pathway to change the orientations of the electric polarization. (c) Energy spectrum of the SnS nanoflakes under states I, II, and III. Red dots for I and III represent the in-gap corner states.

turn to the currently proposed sliding ferroelectricity, which remarkably reveals a universal approach and enables the design of 2D ferroelectric materials out of inherent polar compounds [29,30,72,73]. To date, such a theory has been successfully applied to a bunch of 2D binary compounds XY and transition-metal dichalcogenides XY_2 , such as BN, ZnO, AlN, GaN, SiC, InSe, GaSe, WTe₂, MoS₂, VS₂, and so on [74]. In fact, all of these XY and XY_2 are C_3 -symmetric polar materials, where the electrons transfer from X to Y . Therefore, a large quantized in-plane polarization is generated and drives the Coulomb interaction.

We take boron nitride (BN) as an example, the results of other binary compounds such as ZnO, AlN, GaN, SiC, InSe, and GaSe are given in Fig. 10. The valence atomic configurations for B and N atoms located at 1d and 1f Wyckoff position are $2s_22p_1$ and $2s_22p_3$, respectively, and when forming into the BN compound, all valence electrons of B are moved to the position of N, giving rise to the in-plane electric polarization

along the B-N bond as

$$\mathbf{P} = (1/3, 1/3). \quad (8)$$

Such a quantized polarization is consistent with the results of topological quantum theory,

$$A'_1 @ f + A''_2 @ f + E' @ f, \quad (9)$$

and gives rise to the fractional corner charge for certain terminations. When considering only the $(1/3, 1/3)$ polarization, the Wannier centers move from B atoms to the position of N atoms, leading to a neutral and integer charge configuration, as schematically shown in Fig. 11(a). However, such a configuration is not C_3 symmetric at the corners. To preserve the symmetry, all of the Wannier centers have to be equally distributed over the three sectors, leaving the edge charges in multiples of $e/3$, as illustrated in Fig. 11(b). Moreover, each corner is related to two fractional Wannier centers and thus manifests the corner charges of $2e/3$.

To explicitly prove the existence of fractional corner charges, triangular nanoflakes of BN bilayers were constructed. Figures 11(c) and 11(d) display the energy spectrum and distributions of corner states for the AB and BA stackings, respectively. The bulk energy gaps are clearly visible, and electrons are localized mainly at the C_3 -symmetric corners, revealing the higher-order topology of ferroelectric BN bilayers. However, interestingly, six corner states emerge and arise from both the up and down layers for the BA stacking, while there are only three corner states that emerge mainly on the up layer for the AB stacking. This is due to the fact that for BA stacking both the up and down layers are terminated with zigzag edges of B atoms, while for the AB stacking, the up layer is terminated with zigzag edges of B atoms but the down layer is terminated with armchair edges of N atoms. In addition, with the implementation of an out-of-plane electric field, one can achieve a phase transition between AB and BA stackings. Therefore, the exotic corner states can be controlled so that they are created and annihilated in different layers.

C. Multiferroic materials

In fact, all of the above realizations of ferroelectric HO-TIs are out-of-plane ferroelectric materials with in-plane quantized polarization; we now seek realizations of in-plane ferroelectric materials from the intrinsic multiferroic materials MA ($M = \text{Ge, Sn}$; $A = \text{S, Se}$) [75–78]. As a direct

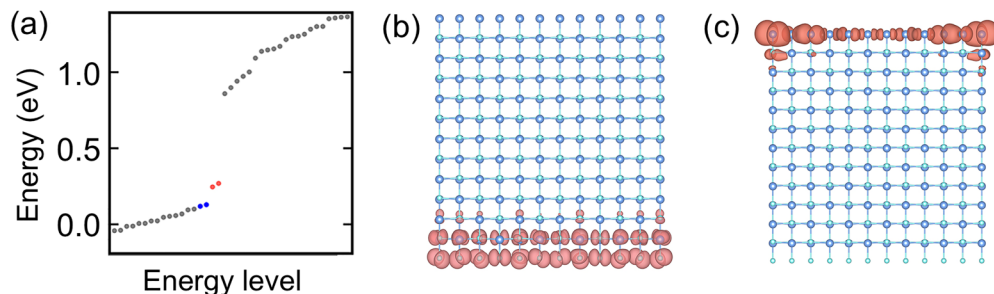


FIG. 13. (a) Energy spectrum of finite nanoflakes for SnS in intermediate state II. The blue and red dots near the Fermi level represent the in-gap edge states, and their distributions are plotted in (b) and (c), respectively.

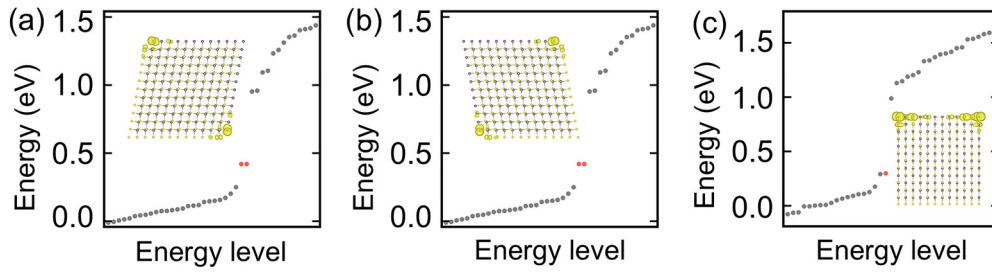


FIG. 14. Energy spectrum of finite nanoflakes for GeS in states (a) I, (b) III, and (c) II. States I and III are the ferroelectric states, with III being the intermediate state. The red dots near the Fermi level represent the in-gap corner states, and the distributions of edge and corner states are plotted in the inset.

consequence of inequivalent lattice constants along the a and b axes, MA have two stable structures, labeled as states I and III, as shown in Fig. 12(a). With the implementation of external in-plane strain or electric field, reversible phase transitions can, indeed, be obtained between states I and III. By means of the nudged elastic band method, the overall ferroelastic switching barrier is calculated and presented in Fig. 12(b); it is almost the same as that of previous theoretical predictions.

To explicitly uncover the HOTI nature, we construct parallelogram nanoflakes of SnS. As shown in Fig. 12(c), two degenerate in-gap states arise around the Fermi level for two ferroelastic states, states I and III, although their accumulations show some differences. Effected by polarization, different corners will exhibit different electric potential, causing energy splitting between corners. However, the top left and bottom right corners of state I, related by the rotation symmetry C_{11} , will share an electric potential of the same amplitude. Therefore, the corner states will emerge as a hallmark of HOTIs. Similarly, electrons will accumulate in the top right and bottom left corners of state III, preserving the rotation symmetry $C_{1\bar{1}}$. In contrast, state II has edge states for both the top and bottom edges (see Fig. 13). Moreover, GeS, GeSe, and SnSe have similar higher-order topological phases, as illustrated in Figs. 14–16. Thus, with the application of strain, one can achieve the transport of corner states, which will give rise to many interesting phenomena and applications.

V. CONCLUSIONS

In conclusion, we have devised a different type of functional phase, namely, ferroelectric HOTIs, and demonstrated that the experimentally synthesized 2D ferroelectrics provide

a rich playground to explore. Material candidates include traditional ferroelectrics such as In_2S_3 , In_2Se_3 , In_2Te_3 , SnS, GeS, SnSe, and GeSe and proposed sliding ferroelectrics such as BN, ZnO, AlN, GaN, SiC, InSe, and GaSe. Our studies lay the groundwork for electronically controlled higher-order topological phases and put forward potential material candidates for exploring the intriguing physics.

ACKNOWLEDGMENTS

This work was supported by the National Natural Science Foundation of China (Grants No. 12174220, No. 11904205, and No. 12074217), the Shandong Provincial Natural Science Foundation of China (Grants No. ZR2019QA019 and No. ZR2019MEM013), the Shandong Provincial Key Research and Development Program (Major Scientific and Technological Innovation Project) (Grant No. 2019JZZY010302), and the Qilu Young Scholar Program of Shandong University.

APPENDIX A: DETAILED INFORMATION ABOUT THE QUANTIZATION OF POLARIZATION

In electronic materials, the in-plane polarization \mathbf{P} can be defined as $\mathbf{P} = p_1\mathbf{a}_1 + p_2\mathbf{a}_2$, where \mathbf{a}_1 and \mathbf{a}_2 are primitive lattice vectors. Under a threefold rotation (C_3), the lattice vectors (\mathbf{a}_1 and \mathbf{a}_2) transform into new lattice vectors (\mathbf{a}'_1 and \mathbf{a}'_2) according to $\mathbf{a}'_1 = \mathbf{a}_2 - \mathbf{a}_1$, $\mathbf{a}'_2 = -\mathbf{a}_1$. Then, the in-plane polarization will become $\mathbf{P}' = -p_1\mathbf{a}'_2 + p_2(\mathbf{a}'_1 - \mathbf{a}'_2) = p_2\mathbf{a}'_1 - (p_1 + p_2)\mathbf{a}'_2$. If the materials have C_3 symmetry, the change in polarization after the C_3 symmetry can be equivalent to only $(p_1, p_2) = (p_2, -p_1 - p_2) + (n_1, n_2)$. Here, (n_1, n_2) represents the integer number of the lattice vector. Therefore,

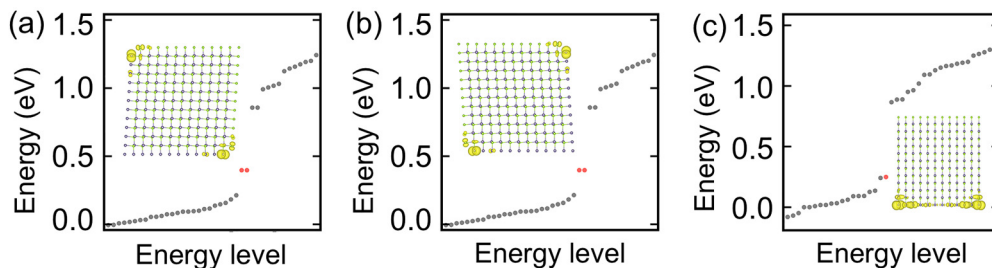


FIG. 15. Energy spectrum of finite nanoflakes for GeSe in states (a) I, (b) III, and (c) II. States I and III are the ferroelectric states, with III being the intermediate state. The red dots near the Fermi level represent the in-gap corner states, and the distributions of edge and corner states are plotted in the inset.

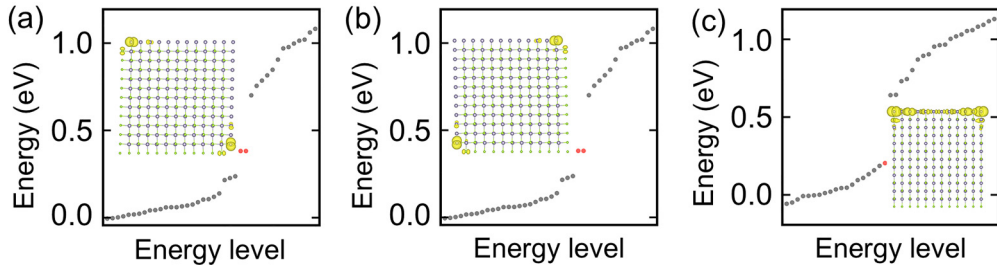


FIG. 16. Energy spectrum of finite nanoflakes for SnSe in states (a) I, (b) III, and (c) II. States I and III are the ferroelectric states, with III being the intermediate state. The red dots near the Fermi level represent the in-gap corner states, and the distributions of edge and corner states are plotted in the inset.

$p_1 = p_2 = n_2/3$, $n_2 = 0, 1, 2$. Similarly, $p_1 = p_2 \in 0, 1/2$ in C_4 -symmetric materials, and $p_1, p_2 \in 0, 1/2$ in C_2 -symmetric materials.

APPENDIX B: DETAILED INFORMATION FOR THE FIRST MODEL HAMILTONIAN

We start from a two-band model on a honeycomb lattice that can be written as

$$H = \sum_i \lambda_i c_i^\dagger c_i + t_1 \sum_{\langle ij \rangle} c_i^\dagger c_j + t_2 \sum_{\langle\langle ij \rangle\rangle} c_i^\dagger c_j + t_3 \sum_{\langle\langle\langle ij \rangle\rangle\rangle} c_i^\dagger c_j. \quad (\text{B1})$$

Here, the first term is the sublattice potential for sublattices A and B . The second, third, and fourth terms represent the nearest-, next-nearest-, and third-nearest-neighbor hoppings.

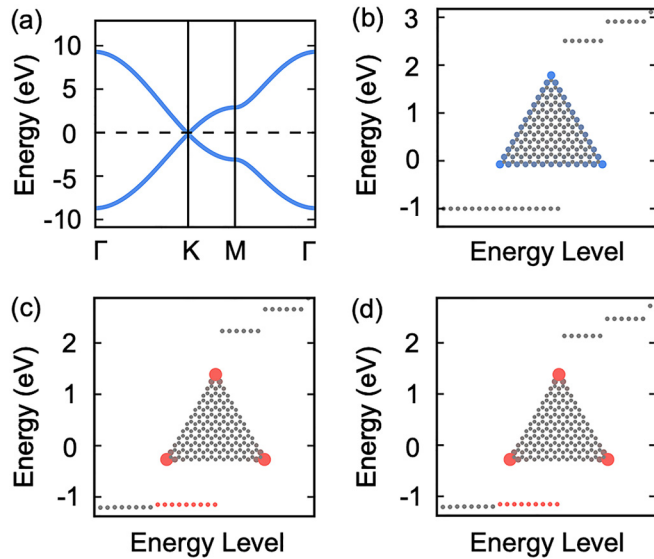


FIG. 17. (a) Band structures of the two-band Hamiltonian without sublattice potential; the Fermi level is indicated with a dashed line. The parameters are set as $\lambda_1 = 0, \lambda_2 = 0, t_1 = -3, t_2 = 0.1$, and $t_3 = 0$. Energy spectrum of the finite nanoflake with sublattice potential when we consider hopping up to (b) nearest neighbors ($\lambda_1 = 2, \lambda_2 = -1, t_1 = -3, t_2 = 0$, and $t_3 = 0$), (c) next-nearest neighbors ($\lambda_1 = 2, \lambda_2 = -1, t_1 = -3, t_2 = 0.1$, and $t_3 = 0$), and (d) third-nearest neighbors ($\lambda_1 = 2, \lambda_2 = -1, t_1 = -3, t_2 = 0.1$, and $t_3 = -0.2$). The red dots near the Fermi level represent the in-gap corner states, and the distributions are plotted in the inset.

When we set the sublattice potential to zero, a gapless crossing point will show up right at the K point, as shown in Fig. 17(a). To obtain an insulator, we have to break the sublattice symmetry, either by the nonzero sublattice potential or by different hopping forms for the next-nearest neighbor. For the first method, we add different kinds of hopping to find a minimal Hamiltonian. As illustrated in Figs. 17(b)–17(d), hopping up to next-nearest neighbor is necessary, whereas the third-nearest-neighbor hopping is not required. As to the second method, we set the sublattice potential to zero. To gap the crossing point, we split the next-nearest-neighbor hopping into two groups with amplitudes t_{2A} and t_{2B} , which represent the hopping from A to A and B to B , respectively. Similar higher-order topological states can be obtained, as shown in Figs. 18(a) and 18(b).

APPENDIX C: DETAILED INFORMATION FOR THE ELEMENTARY BAND REPRESENTATIONS

All of the notations for the elementary band representations are adopted from the Bilbao Crystallographic Server. Below, we give a detailed description of the elementary band representation of Eqs. (6) and (9) in the main text.

For In_2Se_3 , three Se atoms occupy two 1a and one 1c Wyckoff positions, whereas two In atoms occupy 1b and 1c Wyckoff positions. The outer electronic configurations for Se and In atoms are $4s_2p_4$ and $4s_2p_1$, respectively. According to the website of the Bilbao Crystallographic Server [79], the s orbitals in the 1a, 1b, and 1c Wyckoff positions

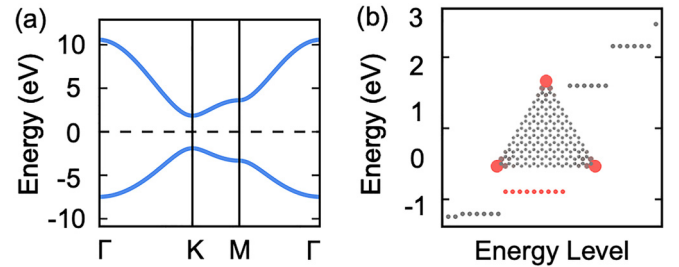


FIG. 18. (a) Band structures of the two-band Hamiltonian without sublattice potential; the Fermi level is indicated with a dashed line. The parameters are set as $\lambda_1 = 0, \lambda_2 = 0, t_1 = -3, t_{2A} = 0.1, t_{2B} = 0.6$, and $t_3 = 0$. (b) Energy spectrum of the finite nanoflake. The red dots near the Fermi level represent the in-gap corner states, and the distributions are plotted in the inset.

transform as the representation of A_1 . Besides, the p orbitals in the 1a, 1b, 1c Wyckoff position transform as the representation of A_1 and E . The decomposition of In_2Se_3 can be written as a combination of elementary band representations, $4A_1@a + 2E@a + 2A_1@c + E@c$. Such a combination can satisfy the electronic configuration of s_2p_6 /empty for Se/In atoms.

For BN, B and N atoms occupy 1d and 1f Wyckoff positions. The outer electronic configurations for Se^{2+} and In^{3-}

atoms are $2s_2p_1$ and $2s_2p_3$, respectively. According to the website of the Bilbao Crystallographic Server, the s orbitals in the 1d and 1f Wyckoff positions transform as the representation of A'_1 . In addition, the p orbitals in the 1d and 1f Wyckoff positions transform as the representation of A'_2 and E' . The decomposition of BN can be written as a combination of elementary band representations, $A'_1@f + A'_2@f + E'@f$. Such a combination can satisfy the electronic configuration of s_2p_6 /empty for B/N atoms.

- [1] X.-L. Qi and S.-C. Zhang, Topological insulators and superconductors, *Rev. Mod. Phys.* **83**, 1057 (2011).
- [2] M. Z. Hasan and C. L. Kane, Colloquium: Topological insulators, *Rev. Mod. Phys.* **82**, 3045 (2010).
- [3] A. Bansil, H. Lin, and T. Das, Colloquium: Topological band theory, *Rev. Mod. Phys.* **88**, 021004 (2016).
- [4] C. L. Kane and E. J. Mele, Quantum Spin Hall Effect in Graphene, *Phys. Rev. Lett.* **95**, 226801 (2005).
- [5] B. A. Bernevig, T. L. Hughes, and S.-C. Zhang, Quantum spin Hall effect and topological phase transition in HgTe quantum wells, *Science* **314**, 1757 (2006).
- [6] C. L. Kane and E. J. Mele, Z_2 Topological Order and the Quantum Spin Hall Effect, *Phys. Rev. Lett.* **95**, 146802 (2005).
- [7] J. Sinova, S. O. Valenzuela, J. Wunderlich, C. H. Back, and T. Jungwirth, Spin Hall effects, *Rev. Mod. Phys.* **87**, 1213 (2015).
- [8] W. A. Benalcazar, B. A. Bernevig, and T. L. Hughes, Quantized electric multipole insulators, *Science* **357**, 61 (2017).
- [9] W. A. Benalcazar, B. A. Bernevig, and T. L. Hughes, Electric multipole moments, topological multipole moment pumping, and chiral hinge states in crystalline insulators, *Phys. Rev. B* **96**, 245115 (2017).
- [10] F. Schindler, A. M. Cook, M. G. Vergniory, Z. Wang, S. S. Parkin, B. A. Bernevig, and T. Neupert, Higher-order topological insulators, *Sci. Adv.* **4**, eaat0346 (2018).
- [11] N. Mao, H. Wang, Y. Dai, B. Huang, and C. Niu, Third-order topological insulators with wallpaper fermions in Tl_4PbTe_3 and Tl_4SnTe_3 , *npj Comput. Mater.* **8**, 154 (2022).
- [12] N. Mao, R. Li, Y. Dai, B. Huang, B. Yan, and C. Niu, Orbital shift-induced boundary obstructed topological materials with a large energy gap, *Adv. Sci.* **9**, 2202564 (2022).
- [13] Z. Song, T. Zhang, Z. Fang, and C. Fang, Quantitative mappings between symmetry and topology in solids, *Nat. Commun.* **9**, 3530 (2018).
- [14] H. C. Po, A. Vishwanath, and H. Watanabe, Symmetry-based indicators of band topology in the 230 space groups, *Nat. Commun.* **8**, 50 (2017).
- [15] F. Tang, H. C. Po, A. Vishwanath, and X. Wan, Topological materials discovery by large-order symmetry indicators, *Sci. Adv.* **5**, eaau8725 (2019).
- [16] M. Ezawa, Topological Switch between Second-Order Topological Insulators and Topological Crystalline Insulators, *Phys. Rev. Lett.* **121**, 116801 (2018).
- [17] Y. Xu, Z. Song, Z. Wang, H. Weng, and X. Dai, Higher-Order Topology of the Axion Insulator EuIn_2As_2 , *Phys. Rev. Lett.* **122**, 256402 (2019).
- [18] C. Yue, Y. Xu, Z. Song, H. Weng, Y. M. Lu, C. Fang, and X. Dai, Symmetry-enforced chiral hinge states and surface quantum anomalous Hall effect in the magnetic axion insulator $\text{Bi}_{2-x}\text{Sm}_x\text{Se}_3$, *Nat. Phys.* **15**, 577 (2019).
- [19] M. J. Park, Y. Kim, G. Y. Cho, and S. B. Lee, Higher-Order Topological Insulator in Twisted Bilayer Graphene, *Phys. Rev. Lett.* **123**, 216803 (2019).
- [20] X.-L. Sheng, C. Chen, H. Liu, Z. Chen, Z.-M. Yu, Y. X. Zhao, and S. A. Yang, Two-Dimensional Second-Order Topological Insulator in Graphdiyne, *Phys. Rev. Lett.* **123**, 256402 (2019).
- [21] B. Liu, G. Zhao, Z. Liu, and Z. Wang, Two-dimensional quadrupole topological insulator in γ -graphyne, *Nano Lett.* **19**, 6492 (2019).
- [22] E. Lee, R. Kim, J. Ahn, and B.-J. Yang, Two-dimensional higher-order topology in monolayer graphdiyne, *npj Quantum Mater.* **5**, 1 (2020).
- [23] C. Chen, Z. Song, J.-Z. Zhao, Z. Chen, Z.-M. Yu, X.-L. Sheng, and S. A. Yang, Universal Approach to Magnetic Second-Order Topological Insulator, *Phys. Rev. Lett.* **125**, 056402 (2020).
- [24] Y. Ren, Z. Qiao, and Q. Niu, Engineering Corner States from Two-Dimensional Topological Insulators, *Phys. Rev. Lett.* **124**, 166804 (2020).
- [25] F. Schindler, Z. Wang, M. G. Vergniory, A. M. Cook, A. Murani, S. Sengupta, A. Y. Kasumov, R. Deblock, S. Jeon, I. Drozdov, H. Bouchiat, S. Guéron, A. Yazdani, B. A. Bernevig, and T. Neupert, Higher-order topology in bismuth, *Nat. Phys.* **14**, 918 (2018).
- [26] Y. B. Choi, Y. Xie, C. Z. Chen, J. Park, S. B. Song, J. Yoon, B. J. Kim, T. Taniguchi, K. Watanabe, J. Kim, K. C. Fong, M. N. Ali, K. T. Law, and G. H. Lee, Evidence of higher-order topology in multilayer WTe_2 from Josephson coupling through anisotropic Hinge states, *Nat. Mater.* **19**, 974 (2020).
- [27] R. Noguchi *et al.*, Evidence for a higher-order topological insulator in a three-dimensional material built from van der Waals stacking of bismuth-halide chains, *Nat. Mater.* **20**, 473 (2021).
- [28] J. Valasek, Piezo-electric and allied phenomena in rochelle salt, *Phys. Rev.* **17**, 475 (1921).
- [29] Z. Guan, H. Hu, X. Shen, P. Xiang, N. Zhong, J. Chu, and C. Duan, Recent progress in two-dimensional ferroelectric materials, *Adv. Electron. Mater.* **6**, 1900818 (2020).
- [30] M. Wu, Two-dimensional van der Waals ferroelectrics: Scientific and technological opportunities, *ACS Nano* **15**, 9229 (2021).
- [31] N. A. Spaldin, A Beginner's guide to the modern theory of polarization, *J. Solid State Chem.* **195**, 2 (2012).
- [32] S. Liu, Y. Kim, L. Z. Tan, and A. M. Rappe, Strain-induced ferroelectric topological insulator, *Nano Lett.* **16**, 1663 (2016).

- [33] B. Monserrat, J. W. Bennett, K. M. Rabe, and D. Vanderbilt, Antiferroelectric Topological Insulators in Orthorhombic AMgBi Compounds ($A = \text{Li, Na, K}$), *Phys. Rev. Lett.* **119**, 036802 (2017).
- [34] L. Kou, H. Fu, Y. Ma, B. Yan, T. Liao, A. Du, and C. Chen, Two-dimensional ferroelectric topological insulators in functionalized atomically thin bismuth layers, *Phys. Rev. B* **97**, 075429 (2018).
- [35] Z. Fei, W. Zhao, T. A. Palomaki, B. Sun, M. K. Miller, Z. Zhao, J. Yan, X. Xu, and D. H. Cobden, Ferroelectric switching of a two-dimensional metal, *Nature (London)* **560**, 336 (2018).
- [36] H. Bai, X. Wang, W. Wu, P. He, Z. Xu, S. A. Yang, and Y. Lu, Nonvolatile ferroelectric control of topological states in two-dimensional heterostructures, *Phys. Rev. B* **102**, 235403 (2020).
- [37] D.-F. Shao, J. Ding, G. Gurung, S.-H. Zhang, and E. Y. Tsymlal, Interfacial Crystal Hall Effect Reversible by Ferroelectric Polarization, *Phys. Rev. Appl.* **15**, 024057 (2021).
- [38] J. Huang, X. Duan, S. Jeon, Y. Kim, J. Zhou, J. Li, and S. Liu, On-demand quantum spin Hall insulators controlled by two-dimensional ferroelectricity, *Mater. Horiz.* **9**, 1440 (2022).
- [39] P. Sharma, F.-X. Xiang, D.-F. Shao, D. Zhang, E. Y. Tsymlal, A. R. Hamilton, and J. Seidel, A room-temperature ferroelectric semimetal, *Sci. Adv.* **5**, eaax5080 (2019).
- [40] S. Dong, J.-M. Liu, S.-W. Cheong, and Z. Ren, Multiferroic materials and magnetoelectric physics: Symmetry, entanglement, excitation, and topology, *Adv. Phys.* **64**, 519 (2015).
- [41] S. Dong and J.-M. Liu, Recent progress of multiferroic perovskite manganites, *Mod. Phys. Lett.* **26**, 1230004 (2012).
- [42] X. Qi, J. Zhou, Z. Yue, Z. Gui, L. Li, and S. Buddhudu, A ferroelectric ferromagnetic composite material with significant permeability and permittivity, *Adv. Funct. Mater.* **14**, 920 (2004).
- [43] X. Liu, A. P. Pyatakov, and W. Ren, Magnetoelectric Coupling in Multiferroic Bilayer VS₂, *Phys. Rev. Lett.* **125**, 247601 (2020).
- [44] C. Xu, P. Chen, H. Tan, Y. Yang, H. Xiang, and L. Bellaiche, Electric-Field Switching of Magnetic Topological Charge in Type-I Multiferroics, *Phys. Rev. Lett.* **125**, 037203 (2020).
- [45] V. Garcia, M. Bibes, L. Bocher, S. Valencia, F. Kronast, A. Crassous, X. Moya, S. Enouz-Vedrenne, A. Gloter, D. Imhoff, C. Deranlot, N. D. Mathur, S. Fusil, K. Bouzouhane, and A. Barthélémy, Ferroelectric control of spin polarization, *Science* **327**, 1106 (2010).
- [46] Y. Liang, N. Mao, Y. Dai, L. Kou, B. Huang, and Y. Ma, Intertwined ferroelectricity and topological state in two-dimensional multilayer, *npj Comput. Mater.* **7**, 1 (2021).
- [47] B. Bradlyn, L. Elcoro, J. Cano, M. G. Vergniory, Z. Wang, C. Felser, M. I. Aroyo, and B. A. Bernevig, Topological quantum chemistry, *Nature (London)* **547**, 298 (2017).
- [48] J. Cano, B. Bradlyn, Z. Wang, L. Elcoro, M. G. Vergniory, C. Felser, M. I. Aroyo, and B. A. Bernevig, Topology of Disconnected Elementary Band Representations, *Phys. Rev. Lett.* **120**, 266401 (2018).
- [49] Y. Xu, L. Elcoro, G. Li, Z.-D. Song, N. Regnault, Q. Yang, Y. Sun, S. Parkin, C. Felser, and B. A. Bernevig, Three-dimensional real space invariants, obstructed atomic insulators and a new principle for active catalytic sites, [arXiv:2111.02433](https://arxiv.org/abs/2111.02433).
- [50] Y. Xu, L. Elcoro, Z.-D. Song, M. Vergniory, C. Felser, S. S. Parkin, N. Regnault, J. L. Mañes, and B. A. Bernevig, Filling-enforced obstructed atomic insulators, [arXiv:2106.10276](https://arxiv.org/abs/2106.10276).
- [51] A. Nelson, T. Neupert, T. Bzdušek, and A. Alexandradinata, Multicellularity of Delicate Topological Insulators, *Phys. Rev. Lett.* **126**, 216404 (2021).
- [52] F. Schindler and B. A. Bernevig, Noncompact atomic insulators, *Phys. Rev. B* **104**, L201114 (2021).
- [53] J. Gao, Y. Qian, H. Jia, Z. Guo, Z. Fang, M. Liu, H. Weng, and Z. Wang, Unconventional materials: The mismatch between electronic charge centers and atomic positions, *Sci. Bull.* **67**, 598 (2022).
- [54] G. Li, Y. Xu, Z. Song, Q. Yang, Y. Zhang, J. Liu, U. Gupta, V. Süß, Y. Sun, P. Sessi, S. S. P. Parkin, B. A. Bernevig, and C. Felser, Obstructed surface states as the descriptor for predicting catalytic active sites in inorganic crystalline materials, *Adv. Mater.* **34**, 2201328 (2022).
- [55] J. P. Perdew, K. Burke, and M. Ernzerhof, Generalized Gradient Approximation Made Simple, *Phys. Rev. Lett.* **77**, 3865 (1996).
- [56] G. Kresse and J. Furthmüller, Efficient iterative schemes for *ab initio* total-energy calculations using a plane-wave basis set, *Phys. Rev. B* **54**, 11169 (1996).
- [57] FLEUR, <http://www.flapw.de>.
- [58] G. Pizzi *et al.*, Wannier90 as a community code: New features and applications, *J. Phys.: Condens. Matter* **32**, 165902 (2020).
- [59] A. A. Mostofi, J. R. Yates, Y.-S. Lee, I. Souza, D. Vanderbilt, and N. Marzari, Wannier90: A tool for obtaining maximally-localised Wannier functions, *Comput. Phys. Commun.* **178**, 685 (2008).
- [60] F. Freimuth, Y. Mokrousov, D. Wortmann, S. Heinze, and S. Blügel, Maximally localized Wannier functions within the FLAPW formalism, *Phys. Rev. B* **78**, 035120 (2008).
- [61] Q. Wu, S. Zhang, H.-F. Song, M. Troyer, and A. A. Soluyanov, Wanniertools: An open-source software package for novel topological materials, *Comput. Phys. Commun.* **224**, 405 (2018).
- [62] J. Gao, Q. Wu, C. Persson, and Z. Wang, Irvsp: To obtain irreducible representations of electronic states in the VASP, *Comput. Phys. Commun.* **261**, 107760 (2021).
- [63] W. A. Benalcazar, T. Li, and T. L. Hughes, Quantization of fractional corner charge in C_n -symmetric higher-order topological crystalline insulators, *Phys. Rev. B* **99**, 245151 (2019).
- [64] R. B. Jacobs-Gedrim, M. Shanmugam, N. Jain, C. A. Durcan, M. T. Murphy, T. M. Murray, R. J. Matyi, R. L. Moore, and B. Yu, Extraordinary photoresponse in two-dimensional In₂Se₃ nanosheets, *ACS Nano* **8**, 514 (2014).
- [65] W. Ding, J. Zhu, Z. Wang, Y. Gao, D. Xiao, Y. Gu, Z. Zhang, and W. Zhu, Prediction of intrinsic two-dimensional ferroelectrics in In₂Se₃ and other III₂-VI₃ van der Waals materials, *Nat. Commun.* **8**, 14956 (2017).
- [66] C. Cui, W.-J. Hu, X. Yan, C. Addiego, W. Gao, Y. Wang, Z. Wang, L. Li, Y. Cheng, P. Li, X. Zhang, H. N. Alshareef, T. Wu, W. Zhu, X. Pan, and L.-J. Li, Intercorrelated in-plane and out-of-plane ferroelectricity in ultrathin two-dimensional layered semiconductor In₂Se₃, *Nano Lett.* **18**, 1253 (2018).
- [67] X. Tao and Y. Gu, Crystalline–crystalline phase transformation in two-dimensional In₂Se₃ thin layers, *Nano Lett.* **13**, 3501 (2013).
- [68] L. Ju, X. Tan, X. Mao, Y. Gu, S. Smith, A. Du, Z. Chen, C. Chen, and L. Kou, Controllable CO₂ electrocatalytic reduction via ferroelectric switching on single atom anchored In₂Se₃ monolayer, *Nat. Commun.* **12**, 5128 (2021).

- [69] Z. Zhang, J. Nie, Z. Zhang, Y. Yuan, Y.-S. Fu, and W. Zhang, Atomic visualization and switching of ferroelectric order in β - In_2Se_3 films at the single layer limit, *Adv. Mater.* **34**, 2106951 (2022).
- [70] J. Zhou, Q. Zeng, D. Lv, L. Sun, L. Niu, W. Fu, F. Liu, Z. Shen, C. Jin, and Z. Liu, Controlled synthesis of high-quality monolayered α - In_2Se_3 via physical vapor deposition, *Nano Lett.* **15**, 6400 (2015).
- [71] D. Wu, Y. Zhou, Y. Zhu, Y. Cho, Q. He, X. Yang, K. Herrera, Z. Chu, Y. Han, M. C. Downer, H. Peng, and K. Lai, Out-of-plane piezoelectricity and ferroelectricity in layered α - In_2Se_3 nanoflakes, *Nano Lett.* **17**, 5508 (2017).
- [72] X. Ma, C. Liu, W. Ren, and S. A. Nikolaev, Tunable vertical ferroelectricity and domain walls by interlayer sliding in β - ZrI_2 , *npj Comput. Mater.* **7**, 177 (2021).
- [73] K. Yasuda, X. Wang, K. Watanabe, T. Taniguchi, and P. Jarillo-Herrero, Stacking-engineered ferroelectricity in bilayer boron nitride, *Science* **372**, 1458 (2021).
- [74] L. Li and M. Wu, Binary compound bilayer and multilayer with vertical polarizations: Two-dimensional ferroelectrics, multiferroics, and nanogenerators, *ACS Nano* **11**, 6382 (2017).
- [75] M. Wu and X. C. Zeng, Intrinsic ferroelasticity and/or multiferroicity in two-dimensional phosphorene and phosphorene analogues, *Nano Lett.* **16**, 3236 (2016).
- [76] R. Fei, W. Kang, and L. Yang, Ferroelectricity and Phase Transitions in Monolayer Group-IV Monochalcogenides, *Phys. Rev. Lett.* **117**, 097601 (2016).
- [77] N. Higashitarumizu, H. Kawamoto, C.-J. Lee, B.-H. Lin, F.-H. Chu, I. Yonemori, T. Nishimura, K. Wakabayashi, W.-H. Chang, and K. Nagashio, Purely in-plane ferroelectricity in monolayer SnS at room temperature, *Nat. Commun.* **11**, 2428 (2020).
- [78] A. Marrazzo and M. Gibertini, Twist-resilient and robust ferroelectric quantum spin Hall insulators driven by van der Waals interactions, *npj 2D Mater. Appl.* **6**, 30 (2022).
- [79] Bilbao Crystallographic Server, <https://www.cryst.ehu.es/>.